J. Fluid Mech. (2010), *vol.* 642, *pp.* 181–212.
doi:10.1017/S0022112009991704

A coupled time-reversal/complex differentiation method for aeroacoustic sensitivity analysis: towards a source detection procedure

ARIANE DENEUVE, PHILIPPE DRUAULT†, RÉGIS MARCHIANO AND PIERRE SAGAUT

Institut Jean Le Rond d'Alembert, Université Pierre et Marie Curie-Paris 6, 4 place Jussieu, case 162, 75252 Paris Cedex 05, France

(Received 27 November 2008; revised 21 August 2009; accepted 21 August 2009; first published online 2 December 2009)

Defining and identifying the aeroacoustic sources in a turbulent flow is a great challenge especially for noise control strategy. The purpose of the present study consists in proposing a new methodology to localize regions associated with sound generation. These regions are associated, in the present work, with those of high sensitivity of the acoustic field, using the heuristic argument that modifying the flow in these regions would lead to a very significant change in the radiated noise. The proposed method relies on the efficient coupling between the time-reversal theory applied to the Euler equations and the complex differentiation method to compute the sensitivity variable. To the knowledge of the authors, this is the first time that the time-reversal technique is applied to vectorial hydrodynamic equations, in place of the classical scalar wave equation. Subsequently, regions associated with sound generation are related to spatiotemporal events which exhibit the maximum of sensitivity to acoustical disturbances measured in far field. The proposed methodology is then successively tested on three cases for which the nature of the source is different: injection of mass, vibrating surfaces and flow instabilities arising in a plane mixing layer flow. For each test case, the two-dimensional Euler equations are solved using a numerical solver based on a pseudo-characteristics formulation. During these computations flow, variables are stored only at the computational boundaries. These variables are time reversed and relevant information concerning the acoustical disturbances is tagged using complex differentiation in order to lead the sensitivity analysis. The same numerical solver is used to access the evolution of the time-reversed variables. In each test case, the proposed methodology allows to localize successfully zones associated with noise generation.

Key words: aeroacoustics, free shear layers, simulation

1. Introduction

One of the main challenges for the noise control technology deals with the production of noise in a turbulent flow and how aeroacoustic sources can be defined and identified. The very definition of what an acoustic source is an open question, even though this concept is easily understood in a qualitative way and a large amount of works has been devoted to this issue. One of the difficulties faced when trying to define

† Email address for correspondence: philippe.druault@upmc.fr

acoustic sources is that there is a fundamental asymmetry in the acoustic problem. The sound field generated by a source field is unique: once the source is known so is the sound, while the converse is not true, since different flow configurations may lead to identical radiated acoustic fields. The purpose of this paper is not to propose a definition of this concept but to propose a methodology to find the wave origin related to aeroacoustic sources.

A large number of aeroacoustic source definitions has been proposed in the past, none of them being fully satisfactory. Their overall consistency, i.e. their ability to educe the same spatiotemporal events as acoustic sources in a given flow, is still to be assessed in most cases. Existing definitions can be classified into a few families, which are briefly discussed below. The reader is referred to the following references (see Goldstein 1976; Lighthill 1978; Pierce 1989; Dowling & Ffwocs Williams 2000; Howe 2003; Colonius & Lele 2004; Wang, Freund & Lele 2006; Wagner, Hüttl & Sagaut 2007) for a more detailed presentation.

A first way to define an acoustic source relies on the analytical models referred as aeroacoustic analogies. In the early 1950s, Lighthill (1952) developed a theory which states that the sound generation process by aerodynamic fluctuations and far-field radiation can be modelled as quadrupole-type sources contained in a bounded volume V embedded in a homogeneous medium at rest. In practice, the Navier–Stokes equations are rearranged into a form that separates out the linear terms (treated as a free-space wave propagation operator of d'Alembertian type) and the nonlinear terms (treated as sound source terms). The source terms appear as a linear combination of second-order derivatives of a tensor, referred to as the Lighthill tensor. This tensor is therefore commonly interpreted as being the theoretical definition of the equivalent aeroacoustic sources. The resulting radiated acoustic pressure field at position x and time t is then computed *via* the following space–time integral:

$$p'(x,t) = \int_0^t \int_V q(y,\tau) G(x,t|y,\tau) \mathrm{d}y \mathrm{d}\tau + BT, \tag{1.1}$$

where $q(y,\tau)$, $G(x,t|y,\tau)$ and BT are the nonlinear source term, the relevant Green's function and the boundary terms, respectively. Lilley (1974) and many others then extended the Lighthill source term by taking into account additional physical phenomena. Based on a dimensional analysis of the terms in the multipole expansion of the wave equation source term, the physical origin to the noise components can then be deduced. Even if these analogies are widely used to define aerodynamic noise sources, some controversies dealing with the physical meaning of the related source terms have been raised (see Tam 2002; Peake 2004; Spalart 2007). Nevertheless, under certain flow assumptions, these analogies provide meaningful results in term of sound source detection, but they require the foreknowledge of the full aerodynamic field within the source domain. The lack of uniqueness of the associated source definition mentioned above is illustrated here by the integral nature of the solution: different hydrodynamic events may lead to the same value of the integral appearing in the right-hand side of (1.1). The integral nature of the solution also increases the difficulty in the definition of local sources in space and time, since a high value of $q(y,\tau)$ does not necessarily means that hydrodynamic events located at position y at time τ will have an important contribution to the sound received by the listener at location x and time t, since it can be cancelled by contributions of other events at other locations and times. In this sense, even the possible use of integral solutions to define local sources is questionable. Another weakness is that the source term $q(y,\tau)$ appears

as the sum of a large number of terms, and the cancellation problem arises once again. Therefore, isolating each term as a physical source term may be misleading. Consequently, such acoustic analogies may fail to isolate true aeroacoustic sources of the far field noise. Then, it has been observed that the source term leads to a different response as a function of the linearization procedure (see Colonius, Lele & Moin 1997). In this sense, Goldstein (2003) proposed a particular flow decomposition where the sound sources are unambiguously defined on any arbitrary-based ambient flow. Recently, Goldstein & Leib (2008) underlined that an optimal base flow has to be chosen in order to properly define the true sound source and a rigorous methodology has to be followed to minimize approximations and to keep formulas exact.

The second way of defining and detecting the aeroacoustic source consists in extracting the flow region which exhibits the highest correlation with the acoustic signal (see Bogey & Bailly 2007; Jordan & Gervais 2008), resulting in a statistical definition of acoustic sources. The main difficulty relies then in isolating the aerodynamic event which corresponds to the theoretical noise sources. In this approach, the only link of the particular physics of sound waves is that a retarded time is introduced to account for the causality principle. This retarded time is usually estimated considering that the speed of sound is constant and that the flow has no effect on sound wave propagation, corresponding to the implicit use of a free-space wave propagation operator. This statistical analysis can be coupled to modal decompositions of the flow to bridge between aerodynamic events and sound generation (see Druault, Yu & Sagaut 2009).

None of the approaches mentioned above yields a fully general and unique definition of what a noise source is. While acoustic analogies are based on the manipulation of the governing equations of compressible fluid dynamics, the correlation-based approach is based on the intuition that a high statistical correlation can be interpreted as a causal interaction. The last and third way is to solve the inverse problem to identify acoustic sources. This technique has been used for a long time in post-processing of antenna data. Here, the optimal distribution of a fixed number of arbitrarily chosen sources (monopoles, dipoles and/or quadrupoles) is computed solving an inverse problem based on a very simple wave-propagation operator. The rapid progresses in computational fluid dynamics and computational aeroacoustics allow for more accurate solutions of the inverse problem, based on more sophisticated physical models. Putting the emphasis on the computation of the inverse hydrodynamic problem since the issue of noise generation is addressed, one must mention the implicit identification of aeroacoustic sources found in adjoint problem-based control of noise generation. In such an approach, the acoustic source is defined as a hydrodynamic event with respect to which the acoustic field, or at least a part of it, exhibits a maximal sensitivity. The high sensitivity is interpreted here as the signature of a causal process, since a change in the event will result in a significant change in the acoustic field. The sensitivities of the solution are the unknowns of the adjoint system, which appears as a linearized problem in which the information is backward-propagated (see Jameson, Martinelli & Pierce 1998). The efficiency of adjoint-based noise reduction strategy has been assessed recently on academic configurations (see Tam & Auriault 1998; Barone & Lele 2005; Wei & Freund 2006; Spagnoli & Airiau 2008). This approach is considered by some authors as a possible way to analyse acoustic sources, e.g. Colonius & Lele (2004) who note that '*the use of adjoint solutions ... relate source statistics to the statistics of the radiated sound*'. One of the main weaknesses of this approach is that it requires the storage

of the full direct solution, i.e. the storage of the solution at all time steps and at all locations.

The goal of the present paper is to propose a new sensitivity analysis of the aeroacoustic source. We then assume that the acoustic wave origin corresponds to an event for which the acoustic field is highly sensitive, as in adjoint-based methods, but which does not require to store the full direct solution. Only the final field and the boundary values have to be stored. Such sensitivity analysis is based on the coupling of the time-reversal theory and sensitivity analysis *via* the complex differentiation method. It is worth noting that, to the author's knowledge, this is the first use of the time-reversal theory for vectorial hydrodynamic equations, previous works dealing with the scalar wave equation (see Lund & Rojas 1989).

The time-reversal procedure has been widely used in acoustics with the recent introduction of cavity and mirror for time-reversal (see Fink *et al.* 2000). Indeed, the wave equation, which depends only on a single variable (for instance the pressure) is invariant by the time-reversal operation (by changing t into $-t$). Let us consider a wave field inside a volume surrounded by a control surface. If the control surface can record and emit sound waves, it is called a cavity, if only one portion of the surface can be used it is referred to a mirror. The basic idea is to record on a cavity or a mirror the sound waves emanating from the volume. Once the signals have been recorded, they are time reversed and sent back to the volume to localize source or focus energy at a given point. Optimal results are obtained in the case of the cavity because it contains the maximum of information (see Cassereau & Fink 1992). Nevertheless, in many situations the knowledge of the acoustical field on only one portion of space, where out-going waves are dominant, is sufficient to obtain very good results (see Fink *et al.* 2000). One reason for the success of the time-reversal mirrors in acoustics is due to the possibility to make such a set-up in practice. It is not easy to build an apparatus able to record and send signals. In acoustics it is possible, thanks to piezoelectrical transducers and the recent progress in electronics. Many applications rely on this principle in medical therapy, in medical imaging, in telecommunications or in non-destructive evaluation (see Fink *et al.* 2000) and so on. In this paper, we extend this procedure to the Euler equations and used it for the detection of regions associated with sound generation till the work of Squire & Trapp (1998).

It is chosen to illustrate the proposed method using the two-dimensional Euler equations for sake of simplicity. There is no loss of generality in considering only two-dimensional Euler equations, since the extension to the three-dimensional case is straightforward. The propagation of acoustic fluctuations is computed using a numerical solver based on a pseudo-characteristics formulation (see Sesterhenn 2001; Lu & Sagaut 2007*b*) (see § 2.1 for more details). Once the acoustic fluctuations have been extracted at the boundaries of the computational domain, one needs to localize regions associated with sound generation within the computational domain. To this end, an inverse problem is solved using the time-reversal theory (see § 2.2). The time-reversal procedure requires applying a mirror symmetry in time and then to operate backward propagation using the numerical tool used to solve the direct problem. In addition to the time-reversal procedure, a sensitivity analysis of the time-reversed field is carried out in order to detect the regions associated with sound generation. The sensitivity analysis is based on the complex differentiation technique, which is described in § 2.3. The combination of these two techniques is possible, thanks to the use of the numerical solver of the Euler equations which is very versatile to treat boundary conditions. To summarize, the methodology proposed in this paper can be divided into four steps:

(*a*) The direct simulation of the aeroacoustic problem is made by solving the Euler equations with an efficient code (see § 2.1). At the end of this stage, the evolution of all the relevant quantities is known in the computation domain and at its boundaries. Only the information at the boundaries is stored.

(*b*) All the quantities at the boundaries are time reversed in such a way that the invariance of the Euler equations is preserved (see § 2.2).

(*c*) Relevant information concerning the acoustical disturbances is tagged using the complex differentiation in order to lead the sensitivity analysis (see § 2.3).

(*d*) The evolution of the various time-reversed quantities is computed with the numerical solver (see § 2.1). The sensitivity analysis is made automatically during this step, thanks to the complex differentiation technique.

The method is assessed considering several test flows in the second part of the paper. First of all, the case of an injection of mass in the domain is treated. Then, the case of vibrating surfaces is solved with the new methodology. Finally, the methodology is applied to localize the regions associated with sound generation in a plane mixing layer.

2. Numerical methodology for sound generation detection

2.1. *Numerical method*

A numerical code solving the two-dimensional Navier–Stokes equations was previously developed for aeroacoustic analysis (see Lu & Sagaut 2007*a*,*b*). Details on the numerical method used in this computational fluid dynamics (CFD) code can then be found in previous papers (see Lu & Sagaut 2007*a*,*b*). By restricting the model to inviscid fluids, one obtains:

$$\frac{\partial \rho}{\partial t} + \nabla \cdot (\rho \boldsymbol{v}) = 0, \tag{2.1}$$

$$\rho \left(\frac{\partial \boldsymbol{v}}{\partial t} + \boldsymbol{v} \cdot \nabla \boldsymbol{v} \right) = -\nabla p, \tag{2.2}$$

$$\frac{\partial \mathbf{s}}{\partial t} + \boldsymbol{v} \cdot \nabla \mathbf{s} = 0, \tag{2.3}$$

where $\rho(\boldsymbol{x}, t)$, $\boldsymbol{v}(\boldsymbol{x}, t) = (u(\boldsymbol{x}, t), v(\boldsymbol{x}, t))$, $p(\boldsymbol{x}, t)$, $s(\boldsymbol{x}, t)$ are density, velocity, pressure and entropy, respectively.

Briefly, the originality of the numerical method lies in the fact that it is based on the pseudo-characteristic formulation of the convection terms introduced by Sesterhenn (2001), from which it follows that the equations can be recast as (since acoustic waves are investigated, the system is restricted to homoentropic solutions for the sake of simplicity):

$$\frac{\partial p}{\partial t} = -\frac{\rho c}{2}((X^+ + X^-) + (Y^+ + Y^-)), \tag{2.4}$$

$$\frac{\partial u}{\partial t} = -\left(\frac{1}{2}(X^+ - X^-) + Y^u \right), \tag{2.5}$$

$$\frac{\partial v}{\partial t} = -\left(X^v + \frac{1}{2}(Y^+ - Y^-) \right), \tag{2.6}$$

$$\frac{\partial s}{\partial t} = 0 \tag{2.7}$$

in which

$$X^{\pm} = (u \pm c)\left(\frac{1}{\rho c}\frac{\partial p}{\partial x} \pm \frac{\partial u}{\partial x}\right), \tag{2.8}$$

$$Y^{\pm} = (v \pm c)\left(\frac{1}{\rho c}\frac{\partial p}{\partial y} \pm \frac{\partial v}{\partial y}\right), \tag{2.9}$$

$$X^{v} = u\frac{\partial v}{\partial x}, \qquad Y^{u} = v\frac{\partial u}{\partial y}, \tag{2.10}$$

where c denotes the local speed of sound. The perfect gas model is used in the rest of this paper, leading to $c^2 = \gamma p/\rho$. Fluxes with $\pm$ superscripts are related to acoustic waves while the other ones correspond to fluctuations advected by the fluid.

This new decomposition of the pressure, velocity and entropy fluxes enables a very simple and natural use of upwind schemes. To enforce both numerical stability and accuracy for wave propagation problems, a high order upwind dispersion relation preserving (DRP) scheme is used. In the interior nodes the fourth order accurate upwind biased DRP scheme is used and this scheme is modified near the computational domain boundaries (see Lu & Sagaut 2007*b*). Time integration is performed using a third-order total variation diminishing (TVD) Runge–Kutta scheme proposed by Shu & Osher (1989).

One of the main interests of the pseudo-characteristic formulation is that it enables an easy implementation of efficient boundary conditions separating acoustic and hydrodynamic disturbances (see Lu & Sagaut 2007*a*). Two kinds of boundary conditions are used in the problems considered in the present paper:

(i) *Subsonic outflow condition.* The outflow condition is equivalent to putting to zero the values of the incoming disturbances. Thanks to the pseudo-characteristic formulation, this condition is easily implemented by forcing: (*a*) for the left boundary $X^{+} = 0$, (*b*) for the right boundary $X^{-} = 0$, (*c*) for the bottom boundary $Y^{+} = 0$ and (*d*) for the top boundary $Y^{-} = 0$.

(ii) *Subsonic inflow condition.* Such a condition allows to prescribe flow variables and their corresponding fluxes on the computational boundaries. It can be used when pressure, velocities are known on the whole boundary. For instance, let us assume that $p(x = 0, y, t)$ and $\boldsymbol{v}(x = 0, y, t)$ are known and must be prescribed on the left boundary. It is possible to compute the derivatives of p and $\boldsymbol{v}$ with respect to y and with respect to t. Following the order of computation proposed below, all the fluxes are then computable on the boundary:

$$Y^{\pm} = (v \pm c)\left(\frac{1}{\rho c}\frac{\partial p}{\partial y} \pm \frac{\partial v}{\partial y}\right), \tag{2.11}$$

$$Y^{u} = v\frac{\partial u}{\partial y}, \tag{2.12}$$

$$X^{v} = \frac{1}{2}(Y^{-} - Y^{+}) - \frac{\partial v}{\partial t}, \tag{2.13}$$

$$X^{\pm} = \frac{-1}{2}(Y^{-} + Y^{+} \pm 2Y^{u}) - \frac{1}{\rho c}\frac{\partial p}{\partial t} \pm \frac{\partial u}{\partial t}. \tag{2.14}$$

This procedure is also valid to compute inflow condition on the right boundary. For the bottom and top boundaries, only the order of computation of the fluxes has to

be modified:

$$X^{\pm} = (u \pm c)\left(\frac{1}{\rho c}\frac{\partial p}{\partial x} \pm \frac{\partial u}{\partial x}\right), \tag{2.15}$$

$$X^{v} = u\frac{\partial v}{\partial x}, \tag{2.16}$$

$$Y^{u} = \frac{1}{2}(X^{-} - X^{+}) - \frac{\partial u}{\partial t}, \tag{2.17}$$

$$Y^{\pm} = \frac{-1}{2}(X^{-} + X^{+} \pm 2X^{v}) - \frac{1}{\rho c}\frac{\partial p}{\partial t} \pm \frac{\partial v}{\partial t}. \tag{2.18}$$

2.2. *The time-reversal procedure*

The time-reversal procedure can be applied to the Euler equations. It is based on the fact that time-reversal is one of the discrete symmetries of the isentropic Euler equation, i.e. set of equations (2.1)–(2.3) remains unchanged for the following change of variables:

$$\begin{cases} t & \to -t, \\ \rho(\boldsymbol{x}, t) & \to \rho(\boldsymbol{x}, -t), \\ \boldsymbol{v}(\boldsymbol{x}, t) & \to -\boldsymbol{v}(\boldsymbol{x}, -t), \\ p(\boldsymbol{x}, t) & \to p(\boldsymbol{x}, -t), \\ s(\boldsymbol{x}, t) & \to s(\boldsymbol{x}, -t). \end{cases} \tag{2.19}$$

Note that all the variables are time reversed. Moreover, the direction of the flow velocity has to be reversed to ensure the invariance of the Euler equations. That last point is very important. Indeed, as pointed out by Roux & Fink (1995), without that operation there is a breakdown of the time-reversal invariance. The meaning of these equations is that, by time reversing all the variables, plus reversing the direction of flow velocity, the quantities have to satisfy the same equations as the original ones. As they are time reversed they will evolve as if the original quantities were read backward in time. Even if the symmetry of the Euler equations with respect to the time variable has been known for a long time, this property has not been used in the field of computational aeroacoustics to our knowledge. Previous studies in hydrodynamics (see Roux & Fink 1995; Roux *et al.* 1997) focused on the study of the linear interaction between acoustics and fluid dynamics. Consequently, they relied on a generalized wave equation which includes the fluid motion (see Lund & Rojas 1989) but not on the full Euler equations.

In practice, to implement the time-reversal procedure, all flow variables are stored at the four boundaries of the computational domain during the computation of the direct problem. It is important to note that only storage along boundaries of the domain is required, instead of the full solution storage in adjoint-based methods, leading to a drastic reduction in the memory requirement. All flow variables are also stored at all the grid points of the computational domain at the last time step of the direct problem to get an initial condition for the reversed problem. Then, the information at the boundaries is time reversed and the sign of the velocity is inversed accordingly to (2.19). The computational box is initialized with the quantities stored at the last iteration with an inversion of sign of the velocity. To impose the reversed boundary condition, the subsonic inflow conditions are chosen (see § 2.1). The variables imposed at the boundaries of the computational domain are then: $\rho(\boldsymbol{x}, \bar{t})$, $-\boldsymbol{v}(\boldsymbol{x}, \bar{t})$, $p(\boldsymbol{x}, \bar{t})$ and

$s(\boldsymbol{x}, \bar{t})$, where $\bar{t}$ is equal to $T - t$ with T the total duration of the simulation in the direct sense.

2.3. *Sensitivity analysis based on complex differentiation*

Even though the time-reversal procedure allows to know the backward evolution in time, it is difficult to educe the acoustic disturbances from the aerodynamic ones and to localize regions associated with sound generation. This is the reason why it is coupled with a technique of sensitivity analysis. Sensitivity analysis becomes an important item in CFD methods due to the great development of applications related to aerodynamic design, stability and control. Several techniques are available for such sensitivity analysis. In this work, we focus on the complex differentiation method, which was suggested in 1967 by Lyness & Moler (1967) and was poorly exploited until the work of Squire & Trapp (1998). The potential of this technique is now recognized and it has already been used for sensitivity studies in computational fluid dynamics (see Vatsa 2000; Anderson *et al.* 2001; Leclerc, Sagaut & Mohammadi 2006; Lu & Sagaut 2007*b*). It relies on the observation that both the direct and the tangent problems can be solved at the same time by just extending the governing equations in the complex domain, the real and the imaginary parts being associated with the direct and tangent problems, respectively.

Briefly, the complex differentiation relies on the Taylor expansion of a function f, which is real on the real axis, and has a small imaginary part denoted ϵ:

$$f(x + \mathrm{i}\epsilon) = f(x) + \mathrm{i}\epsilon f'(x) - \epsilon^2 \frac{f''(x)}{2} + O(\epsilon^3), \tag{2.20}$$

where $\mathrm{i}^2 = -1$ is the imaginary complex number. Consequently, the first derivative of the complex function f can be expressed, thanks to the imaginary part of function f:

$$f'(x) = \frac{\mathrm{Im}\ [f(x + \mathrm{i}\epsilon)]}{\epsilon} + O(\epsilon^2). \tag{2.21}$$

That last expression provides an alternative method to compute the derivative of f with no numerical derivative, thus no spatial-discretization errors. The truncation error of the derivative is of the order of the square of ϵ. The real part of the function is a second- order approximation of the original function:

$$f(x) = \mathrm{Re}[f(x + \mathrm{i}\epsilon)] + O(\epsilon^2). \tag{2.22}$$

An elegant implementation of this approach consists in changing real variables into complex ones in the numerical solver. This is the only thing to do to implement the complex differentiation method. It has already been done in a previous study (see Lu & Sagaut 2007*a*) in which it was shown that complex differentiation permits to track the hydrodynamic part of a flow as well as the acoustic one.

Let us denote with a tilde the imaginary part of each flow variables : $\rho(\boldsymbol{x}, t) \rightarrow \rho(\boldsymbol{x}, t) + \mathrm{i}\epsilon\tilde{\rho}(\boldsymbol{x}, t)$, $\boldsymbol{v}(\boldsymbol{x}, t) \rightarrow \boldsymbol{v}(\boldsymbol{x}, t) + \mathrm{i}\epsilon\tilde{\boldsymbol{v}}(\boldsymbol{x}, t)$, $p(\boldsymbol{x}, t) \rightarrow p(\boldsymbol{x}, t) + \mathrm{i}\epsilon\tilde{p}(\boldsymbol{x}, t)$ and $s(\boldsymbol{x}, t) \rightarrow s(\boldsymbol{x}, t) + \mathrm{i}\epsilon\tilde{s}(\boldsymbol{x}, t)$. It is important to note that tilded quantities are the sensitivities of the physical variables. By inserting these relations into (2.4)–(2.7), one obtains the complex Euler equations. The real part provides a second-order approximation of the direct problem:

$$\frac{\partial p}{\partial t} + \frac{\rho c}{2}((X^+ + X^-) + (Y^+ + Y^-)) = O(\epsilon^2), \tag{2.23}$$

$$\frac{\partial u}{\partial t} + \left(\frac{1}{2}(X^+ - X^-) + Y^u\right) = O(\epsilon^2), \tag{2.24}$$

$$\frac{\partial v}{\partial t} + \left(X^v + \frac{1}{2}(Y^+ - Y^-)\right) = O(\epsilon^2), \tag{2.25}$$

while the imaginary part is a second-order approximation of the linear tangent problem:

$$\frac{\partial \tilde{p}}{\partial t} + \left(\frac{\tilde{\rho}c + \rho\tilde{c}}{2}\right)((X^+ + X^-) + (Y^+ + Y^-)) + \frac{\rho c}{2}((\tilde{X}^+ + \tilde{X}^-) + (\tilde{Y}^+ + \tilde{Y}^-)) = O(\epsilon^2), \tag{2.26}$$

$$\frac{\partial \tilde{u}}{\partial t} + \left(\frac{1}{2}(\tilde{X}^+ - \tilde{X}^-) + \tilde{Y}^u\right) = O(\epsilon^2), \tag{2.27}$$

$$\frac{\partial \tilde{v}}{\partial t} + \left(\tilde{X}^v + \frac{1}{2}(\tilde{Y}^+ - \tilde{Y}^-)\right) = O(\epsilon^2), \tag{2.28}$$

in which

$$\tilde{X}^{\pm} = (\tilde{u} \pm \tilde{c})\left(\frac{1}{\rho c}\frac{\partial p}{\partial x} \pm \frac{\partial u}{\partial x}\right) + (u \pm c)\left(\widetilde{\left(\frac{1}{\rho c}\right)}\frac{\partial p}{\partial x} + \frac{1}{\rho c}\frac{\partial \tilde{p}}{\partial x} \pm \frac{\partial \tilde{u}}{\partial x}\right), \tag{2.29}$$

$$Y^{\pm} = (\tilde{v} \pm \tilde{c})\left(\frac{1}{\rho c}\frac{\partial p}{\partial y} \pm \frac{\partial v}{\partial y}\right) + (v \pm c)\left(\widetilde{\left(\frac{1}{\rho c}\right)}\frac{\partial p}{\partial y} + \frac{1}{\rho c}\frac{\partial \tilde{p}}{\partial y} \pm \frac{\partial \tilde{v}}{\partial y}\right), \tag{2.30}$$

$$\tilde{X}^v = \tilde{u}\frac{\partial v}{\partial x} + u\frac{\partial \tilde{v}}{\partial x}, \qquad \tilde{Y}^u = \tilde{v}\frac{\partial u}{\partial y} + v\frac{\partial \tilde{u}}{\partial y} \tag{2.31}$$

and $\tilde{c} = \widetilde{\sqrt{\gamma p/\rho}}$.

In practice, the acoustical disturbances are extracted at the boundaries of the computational domain. Complex differentiation is quite versatile and permits to choose the best set of control parameters in each case. For instance, frequency can be a good acoustical tag, so can be spatial position (on one or more boundaries). In all the examples presented in the next section, the set of parameters is given and the choice is discussed. Once the set of parameters is known, a small complex part is added to parameters and/or variables (inside the computational domain or at boundaries) to be monitored.

The equations above must be supplemented by adequate boundary conditions. They are obtained by applying complex differentiation to the original boundary conditions. As an example, the real parts of the complex subsonic inflow conditions on left and right boundaries, which hold for the direct problem, are

$$Y^{\pm} = (v \pm c)\left(\frac{1}{\rho c}\frac{\partial p}{\partial y} \pm \frac{\partial v}{\partial y}\right) + O(\epsilon^2), \tag{2.32}$$

$$Y^u = v\frac{\partial u}{\partial y} + O(\epsilon^2), \tag{2.33}$$

$$X^v = \frac{1}{2}(Y^- - Y^+) - \frac{\partial v}{\partial t} + O(\epsilon^2), \tag{2.34}$$

$$X^{\pm} = \frac{-1}{2}(Y^- + Y^+ \pm 2Y^u) - \frac{1}{\rho c}\frac{\partial p}{\partial t} \pm \frac{\partial u}{\partial t} + O(\epsilon^2). \tag{2.35}$$

The imaginary parts of the inflow conditions, which hold for the sensitivity variables, are (the imaginary parts are still denoted with a tilde)

$$\tilde{Y}^{\pm} = (\tilde{v} \pm \tilde{c})\left(\frac{1}{\rho c}\frac{\partial p}{\partial y} \pm \frac{\partial v}{\partial y}\right) + (v \pm c)\left(\widetilde{\left(\frac{1}{\rho c}\right)}\frac{\partial p}{\partial y} + \frac{1}{\rho c}\frac{\partial \tilde{p}}{\partial y} \pm \frac{\partial \tilde{v}}{\partial y}\right) + O(\epsilon^2), \tag{2.36}$$

$$\tilde{Y}^u = v\frac{\partial \tilde{u}}{\partial y} + \tilde{v}\frac{\partial u}{\partial y}, \tag{2.37}$$

$$\tilde{X}^v = \frac{1}{2}(\tilde{Y}^- - \tilde{Y}^+) - \frac{\partial \tilde{v}}{\partial t} + O(\epsilon^2), \tag{2.38}$$

$$\tilde{X}^{\pm} = \frac{-1}{2}(\tilde{Y}^- + \tilde{Y}^+ \pm 2\tilde{Y}^u) - \widetilde{\left(\frac{1}{\rho c}\right)}\frac{\partial p}{\partial t} - \frac{1}{\rho c}\frac{\partial \tilde{p}}{\partial t} \pm \frac{\partial \tilde{u}}{\partial t} + O(\epsilon^2). \tag{2.39}$$

To ensure the coupling between the time-reversal procedure and the complex differentiation technique, the time-reversal procedure is applied first (defined in (2.19)), then, the complex inflow conditions are prescribed (defined in (2.11)–(2.14)).

3. Results

To assess the potential of the proposed method, three problems associated to different sources of sound have been studied. The first one consists in an injection of mass inside the computational domain. The second one deals with the sound generated at different frequencies by vibrating surfaces. Finally, the methodology is applied to detect the regions associated with sound generation in a spatially developing subsonic plane mixing layer.

3.1. *Sound generation due to mass injection*

Mass injection is known to yield pressure waves in the general case (see Kovasznay 1953; Sagaut & Cambon 2008). The first test case deals with an initial density perturbation in a uniform flow and the second one with a initial density perturbation in a flow with a vortex.

For the first case, the computational domain size is $(0, 10; 0, 10)$ corresponding to a uniform mesh of (100×100) points. An injection of mass is made at $t = 0$. The initial density perturbation profile is an axisymmetric Gaussian one (figure 1*a*) given by

$$\rho(x, y, t = 0) = \rho_0 + a \exp\left(\frac{x^2 + y^2}{\sigma^2}\right), \tag{3.1}$$

where $a = 0.001$ and $\sigma = 0.5$. A uniform flow is imposed, such as $u(x, y, t = 0) = u_0 = 100$ and $v_0 = 0$. The associated Mach number is equal to 0.29. All the boundaries are chosen to be subsonic outflow conditions.

The mass injection initiates an acoustic wave that propagates and expands in time. An illustration is displayed in figure 1, which represents the pressure evolution at three different times. As there exists a flow along the X-axis, the pressure wave is

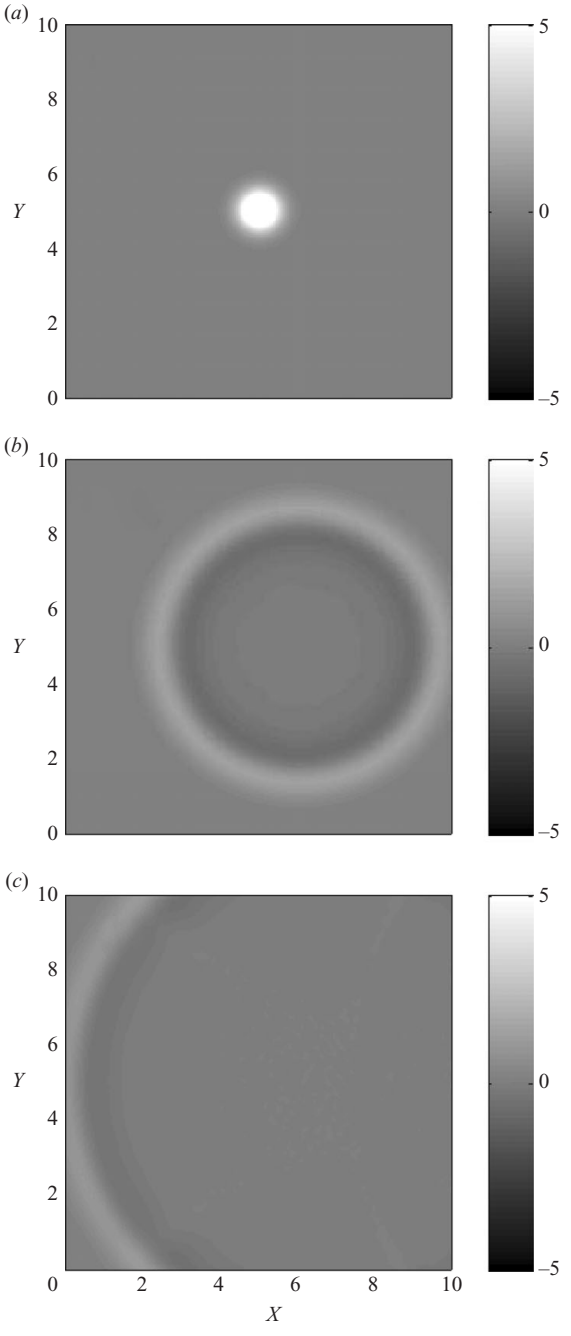

FIGURE 1. Direct simulation of the fluctuations of the pressure field $(p(x, y, t) - P_0)$ for the injection of mass (*a*) $t = 0$, (*b*) $t = 150\Delta t$ and (*c*) $t = 300\Delta t$.

advected. During the computation, at each time step, velocity and pressure fields are stored at the four boundaries. Furthermore, at the end of the computation, the spatial variables are stored at each point of the domain. The total duration of the simulation, $T = 500\Delta t$, where Δt is the time step, is chosen to ensure that most of the fluctuating

energy has left the computational box at the end of the simulation. The time step Δt is fixed to 7.10^{-5} in order to ensure a Courant–Friedrichs–Lewy (CFL) number of the computation inferior to 0.6.

The second step consists in performing the time-reversed simulation of the acoustic pressure pulse. The time-reversal operation is performed on all stored data according to (2.19), like in time-reversal cavity applications. The boundary conditions are now chosen to be inflow conditions. For the moment the complex differentiation is not used. Figure 2 shows the pressure field at three different times (corresponding to those shown in figure 1 but in inverted order). It is clear that the dynamic of the evolution is very well recovered. Indeed, figure 2(a) is similar to the last figure of the simulation in direct sense figure 1(c). The corresponding time is $\bar{t} = 200\Delta t$, this value corresponds to the total duration of the simulation in the direct sense minus the time of the event presented in figure 1(c): $\bar{t} = 200\Delta t = 500\Delta t - 300\Delta t$. It is in agreement with the formula: $\bar{t} = T - t$ with $\bar{t}$ the time of the reversed time simulation, T the total duration in the direct simulation and t the time in the direct simulation. In figure 2(b) it can be seen that the pressure waves retropropagate to the initial position of the spot of mass injection with a very satisfactory accuracy. Finally, figure 2(c) shows that the time-reversal procedure allows to recover the initial spot of mass injected in the computational domain at the correct time. In that example, simulation is stopped at T corresponding to the duration of the direct simulation. Simulation for a time $t > T$ can not be performed because the historical boundary data are unavailable. Furthermore in the time-reversed simulation, no mechanism is implemented to compensate the injection of mass made at $t = 0$ in the direct simulation. Figure 4 provides a comparison of the pressure field at the centre of the computational domain. The differences between the initial distribution of pressure and the result obtained thanks to the time-reversal procedure are very small.

To investigate the robustness of the time-reversal procedure with respect to the completeness of the boundary data, three additional cases have been defined. We propose to use only three, two and one inflow boundaries in the time-reversed simulation instead of the four used in the previous case. Such test cases can be related to time-reversal mirror applications. For the first simulation the time-reversal procedure is made on the top, the bottom and the right boundaries. The left boundary is selected to be of subsonic outflow type. Figure 3 displays the pressure field corresponding to the initial time in the direct sense. Compared to the case in which four inflow boundaries are used, the results are also of good quality, since they permit to predict the location of the mass injection. Nevertheless, as it is shown by figure 4, the amplitude of the pressure field computed by time-reversal procedure is smaller than the original one. The second and third simulations are performed respectively with two and one active inflow boundaries (the top, the bottom ones for the second simulation and only the bottom one for the third simulation). The quality of the results (see figure 3b,c)) is not as good as in the previous cases. In particular, the shape and the strength of the pressure profile are changed as observed in figure 4. The maximum value of the pressure relative error is around 48 % and 73 % for test cases (b) and (c) respectively. Indeed the quantity of energy that retropropagates to the spot of mass injection is less important than in the case where four boundaries are considered. Nevertheless, the location of the spot of mass injection is again satisfactorily predicted. These results show that the time-reversal procedure is a robust method which permits to localize aeroacoustic event generating acoustical waves even if the boundary conditions of the time-reversed simulation are

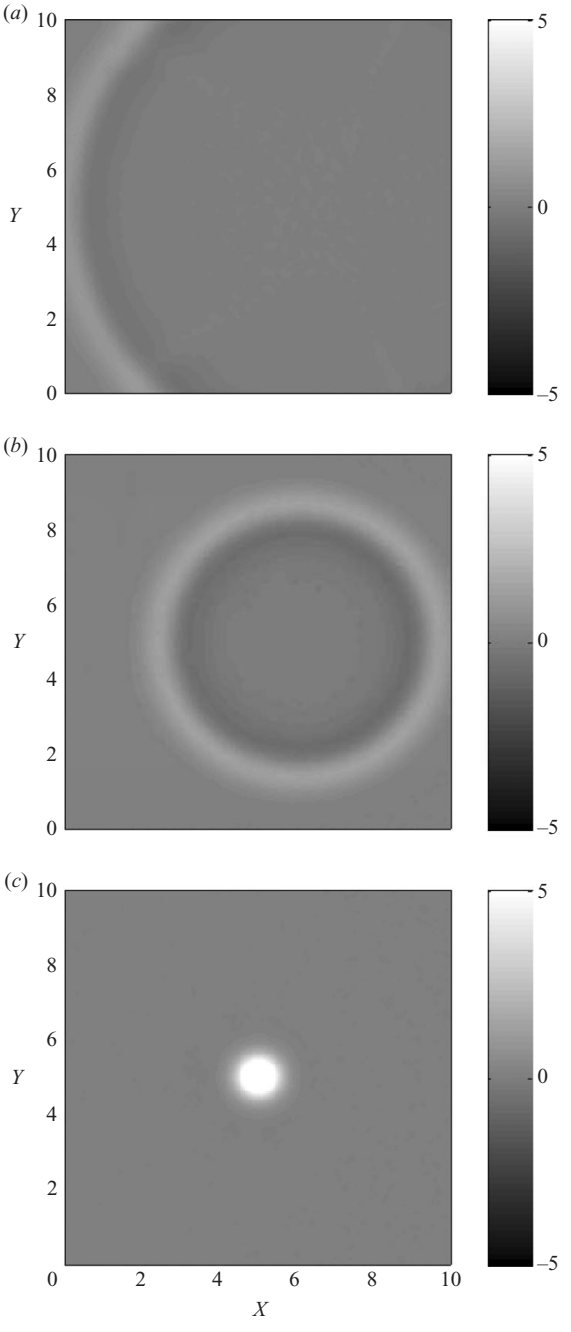

FIGURE 2. Fluctuating pressure field $(p(x, y, t) - P_0)$ computed using the time-reversal procedure in the case in which subsonic inlet conditions are enforced on all four boundaries: (*a*) $\bar{t} = 200\Delta t$, (*b*) $\bar{t} = 350\Delta t$ and (*c*) $\bar{t} = 500\Delta t$.

lacunary. Such a result demonstrates the great potential of the methodology when only a minimal amount of flow information permits to focus on the acoustic region associated with sound generation.

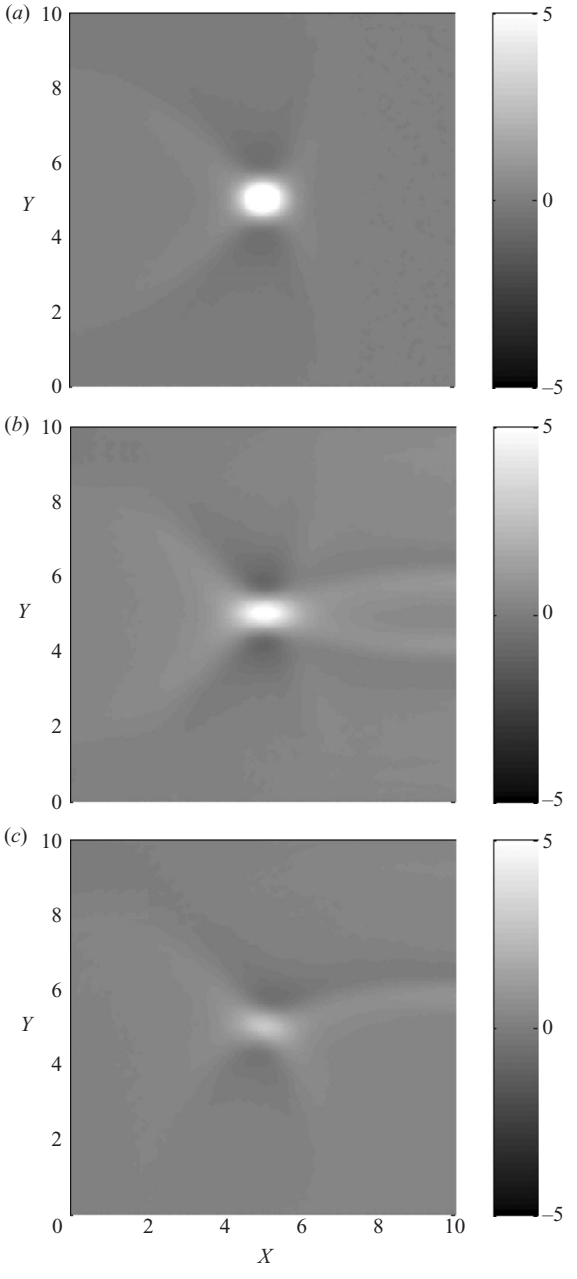

FIGURE 3. Pressure field at $\bar{t} = T$ for three different simulations using the time-reversal procedure on (*a*) three boundaries: the top, the bottom and the right ones; (*b*) two boundaries: the top and the right ones and (*c*) one boundary: the right one.

Nevertheless, to ensure a maximal quality, the time-reversal procedure is applied with complete boundary information in all simulations presented hereafter.

The sensitivity analysis is now carried out using the complex differentiation method explained in § 2.3. The goal of the sensitivity analysis is to compute the sensitivity of

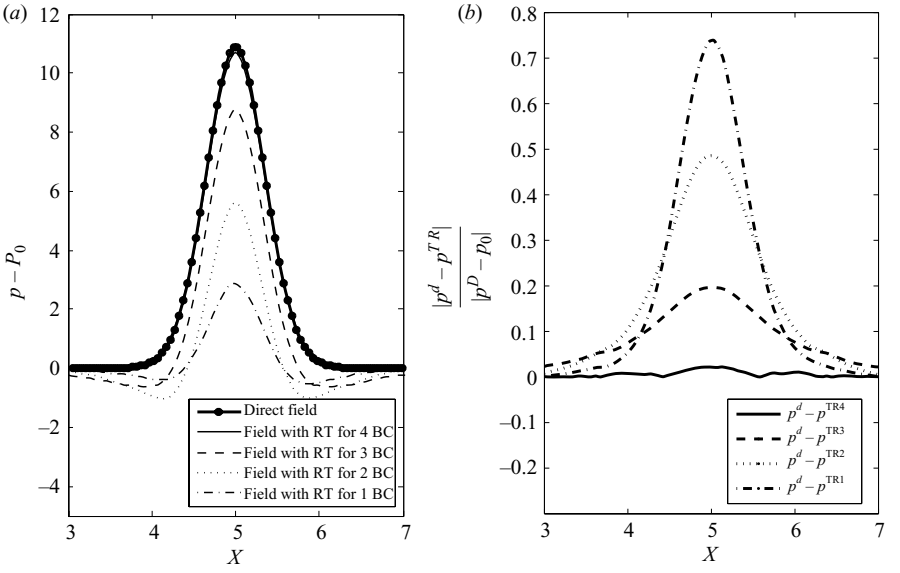

FIGURE 4. (*a*) Fluctuations of the pressure field ($p(x, y = L_y/2, t) - P_0$) at the centre of the computational domain for the direct simulation ($t = 0$) black line and for the time-reversal procedure applied to respectively to 4 ($\bar{t} = T$, thin black line), 3 ($\bar{t} = T$,dash line), 2 ($\bar{t} = T$, dot line) and 1 ($\bar{t} = T$, dash-dot line) boundaries. (*b*) Relative error between the time- reversed simulations and the direct simulation.

the acoustic disturbances. First, the time-reversal procedure is applied on the variables stored on each boundary. Then, an imaginary part is added to the acoustical pressure (already reversed). The magnitude of the imaginary part is taken equal $\epsilon = 1.10^{-6}$, which was shown to ensure an accurate and robust solution (see Lu & Sagaut 2007*a*). At each time step, it is possible to compute the sensibility to the acoustic disturbances by simply monitoring the imaginary part of the pressure field. Figure 5 displays the imaginary part of the pressure field for three different times of the simulation. The chosen times correspond to those of figure 5. It is clear that the maximum of sensitivity corresponds to the acoustic wave at each time. For instance, figure 5(*b*) shows the wavefront responsible of the waves recorded on the boundary of the computational domain. At this time ($\bar{t} = 350\Delta t$), we consider that wavefront is the origin of the sound. We introduce here a distinction between acoustic source and origin of sound. The sensitivity analysis allows us to determine the sensitive areas at a given time and not to provide the physical mechanisms intrinsic to an acoustic source. For the last time, the maximum sensitivity is associated to the spot of mass injected in the direct simulation. This corresponds to the intuitive detection of the origin of the sound wave.

We now assess the robustness of the proposed method in cases exhibiting strong scattering effects. To this end, we consider injection of mass interacting with a steady vortex. This vortex is defined following Taylor's model with an exponentially decaying velocity profile leading to a zero circulation vortex (see Colonius *et al.* 1994). This vortex has a core size of 10 and a Mach number of 0.2. It is generated at the centre of the computational domain. The computational domain size is $(-40, 40; -40, 40)$ corresponding to a uniform mesh of (800×800) points. An injection of mass is made at $t = 0$. The initial density perturbation profile is the same than in the first example

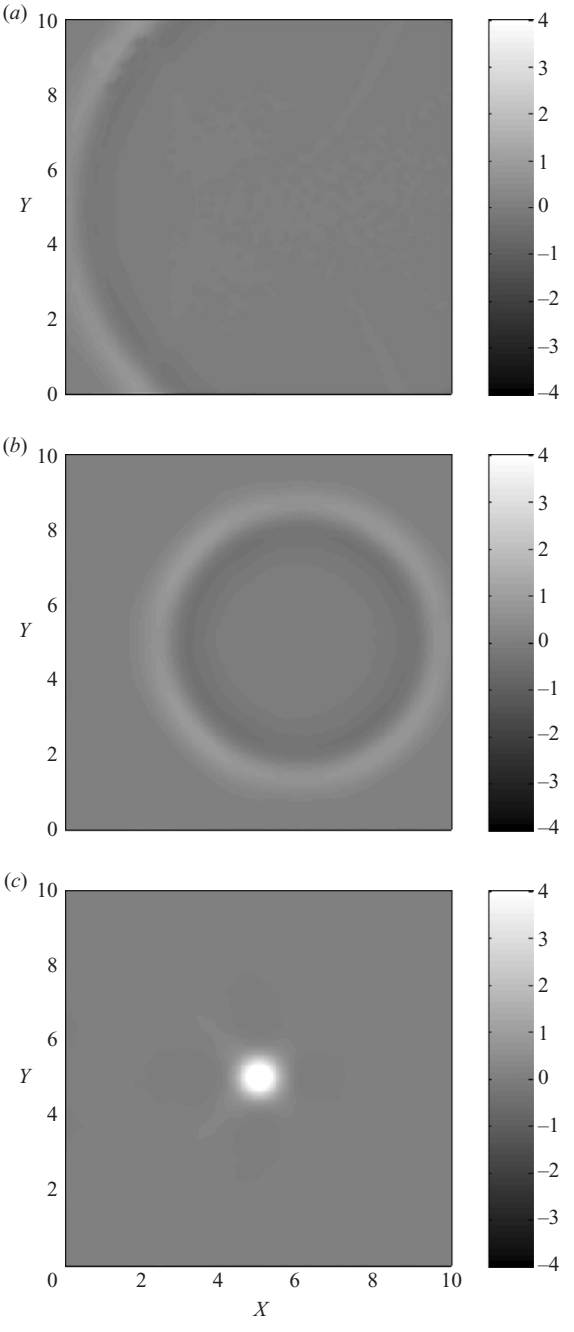

FIGURE 5. Imaginary part of the pressure field for three different times (*a*) $\bar{t} = 200\Delta t$, (*b*) $\bar{t} = 350\Delta t$ and (*c*) $\bar{t} = 500\Delta t$.

(defined in 3.1) except it is located in ($X = -12$, $Y = 0$). All the boundaries are chosen to be subsonic outflow conditions.

Again, the mass injection initiates an acoustic wave that propagates and expands in time (see figure 6). The wavefront propagating through the vortex is dislocated (see

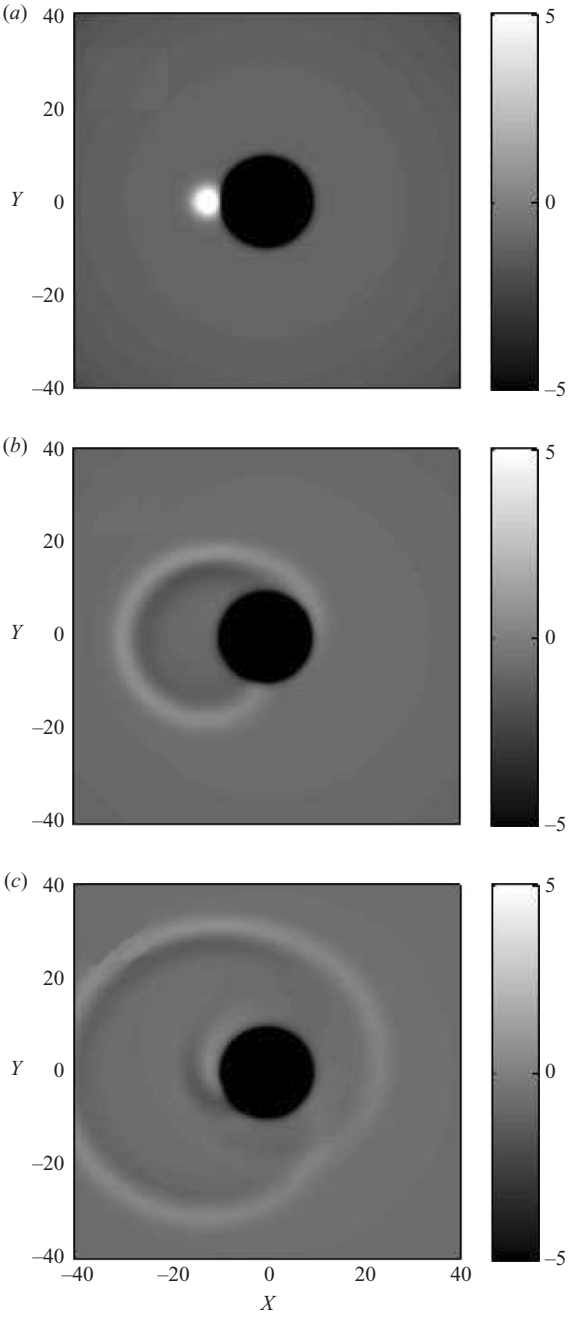

FIGURE 6. Direct simulation of the fluctuating pressure field $(p(x, y, t) - P_0)$ for the interaction of a spot of mass injection and a Taylor vortex: (*a*) $t = 0$, (*b*) $t = 500\Delta t$ and (*c*) $t = 900\Delta t$.

figure 6*b*,*c*)). During the flow simulation, at each time step, Δt, velocity and pressure fields are stored at the four boundaries. Furthermore, at the end of the computation, the spatial variables are stored at each point of the domain. The total duration of the simulation, $T = 1700\Delta t$.

The time-reversal procedure is applied on the data recorded at the four boundaries and at the last time step. The time-reversal simulation of the mass injection in interaction with a steady vortex is now performed. Figure 7 shows three instantaneous fluctuating pressure fields obtained at the same instants than those presented in the last figure deduced from the direct numerical simulation. The procedure is able to localize accurately the position of the initial spot of mass injection even in presence of vorticity. No spurious waves or artefacts are visible from the visualization of the time-reversed data. When comparing the amplitude of the pressure field obtained at the end of the time-reversal simulation to the one of the initial pressure field of the direct simulation, a difference of less than 0.2 % is observed. This test case emphasizes that the methodology is robust for the refraction or scattering problems.

Finally, the complex differentiation technique is used to study the sensitivity with respect to acoustical variables. It then consists in computing the sensitivity analysis of the acoustic wave related to the initial spot of mass injection. Then, before performing the time-reversal simulation, at each computational boundary, a small imaginary part is only added to the acoustic disturbance related to the initial spot of mass injection. Figure 8 shows the imaginary part of the pressure field for the same three different times as in figure 7. On this figure, the contribution of the aerodynamic part of the pressure field, namely the pressure due to the vortex, is not visible. This is because this part of the field is not sensitive to the acoustical variables. The evolution of the imaginary part shows that the maximum coincides with the wavefront, and the retropropagation allows to find the location of the original position of the spot of mass injection. Such sensitivity analysis based on the complex differentiation is then robust even in presence of strong scattering effects.

3.2. *Acoustic wave generation by vibrating surfaces*

Another important kind of acoustic sources deals with the sound produced by vibrating surfaces. In that example, we consider two pistons located on the left boundary of the computational domain with a non-dimensional width taken equal to 2. They emit sinusoidal waves at frequencies f_1 for the first piston and f_1 and f_2 for the second one, so they have one common frequency. It is assumed that the normal velocity between the vibrating surfaces and the fluid is continuous. Consequently the following conditions are imposed (inflow condition) on the left boundary:

$$u(x=0, y, t) = \begin{cases} U_0(\sin(2\pi f_1 t)\ , \text{ if } y \in [2:4], \\ U_0(\sin(2\pi f_1 t) + \sin(2\pi f_2 t))\ , \text{ if } y \in [6:8], \\ 0, \text{ otherwise}, \end{cases} \tag{3.2}$$

with amplitude $U_0 = 2.5 \times 10^{-3}$. Moreover, a linear increasing shear flow in the vertical direction: $u(x, y) = 100 + 10y$ is considered. The computational domain size is 2.5×10. A uniform grid with 100×400 grid points is used. The Mach number is taken equal to 0.29. The CFL number is equal to 0.6, ensuring an accurate representation of physical phenomena.

The pistons emit waves from $t = 0$ to $t = 500\Delta t$. The total duration of the simulation is $T = 1000\Delta t$. Figure 9 shows the instantaneous pressure field issued from the piston at three different times. The fluctuating pressure field is made of two wave packets with partial spatial overlap. As previously described, the variables are stored on each boundary of the computational domain.

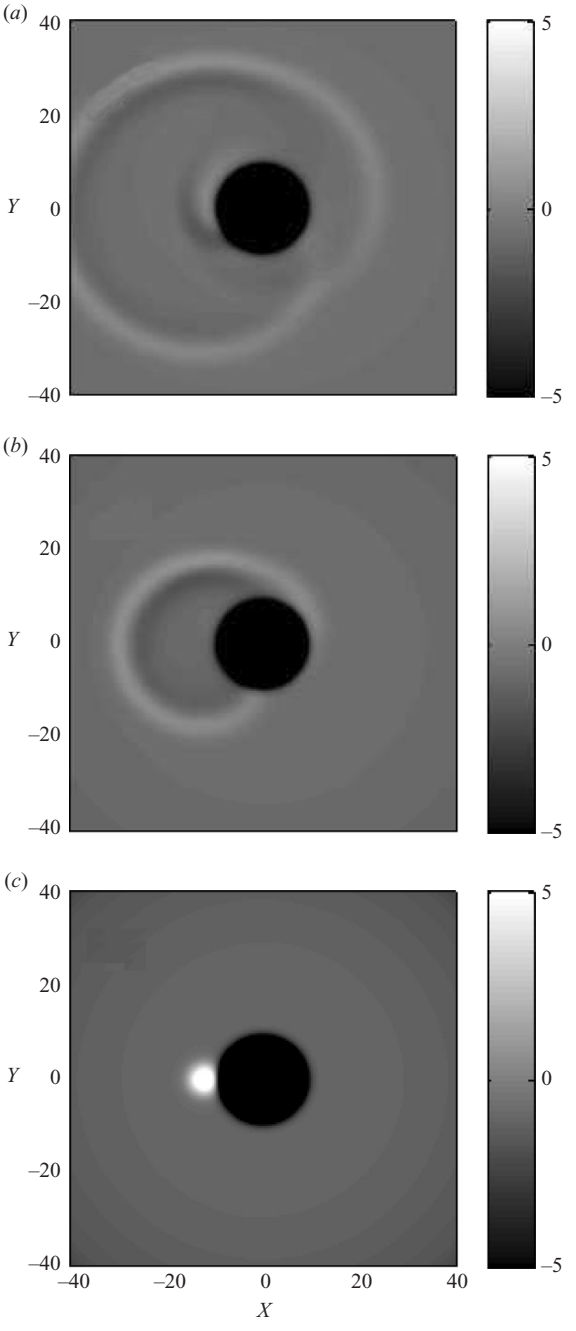

FIGURE 7. Fluctuating pressure field $(p(x, y, t) - P_0)$ computed from the time reversal simulation where subsonic inlet conditions are enforced on all four boundaries: (*a*) $\bar{t} = 800$, (*b*) $\bar{t} = 1200\Delta t$ and (*c*) $\bar{t} = 1700\Delta t$.

The time-reversal procedure is applied to the variables at the boundaries and to the last fields recorded in the direct simulation. Then, an imaginary part is associated to acoustical pressure on the top, the bottom and the right boundaries. These boundaries are now of subsonic inflow type. The left boundary is of subsonic outflow type.

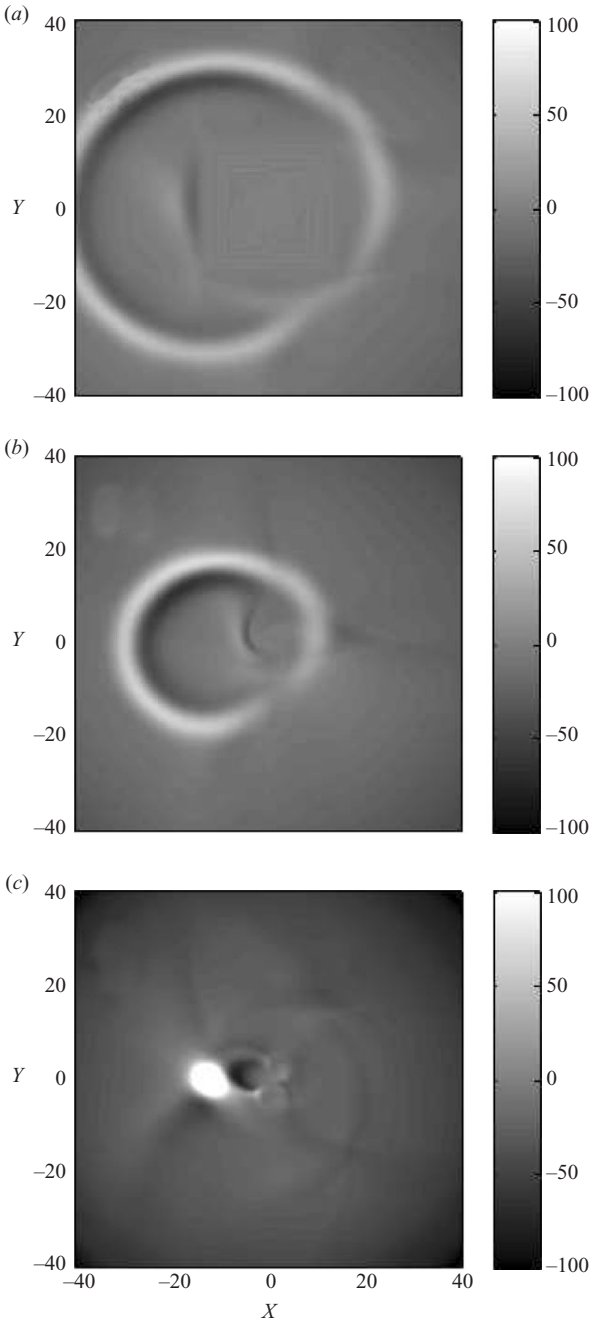

FIGURE 8. Imaginary part of the pressure field for three different times: (*a*) $\bar{t} = 800$, (*b*) $\bar{t} = 1200\Delta t$ and (*c*) $\bar{t} = 1700\Delta t$.

Figure 10 shows the imaginary part of the pressure field computed by the proposed method at three different times $\bar{t} = 400, 700$ and $900\Delta t$. The backward propagation of the pressure waves towards the locations of the pistons is clearly visible. Therefore, both the position and the width of the pistons can be recovered from the sensitivity analysis. Moreover, the sensitivity analysis can be made on the different parts of

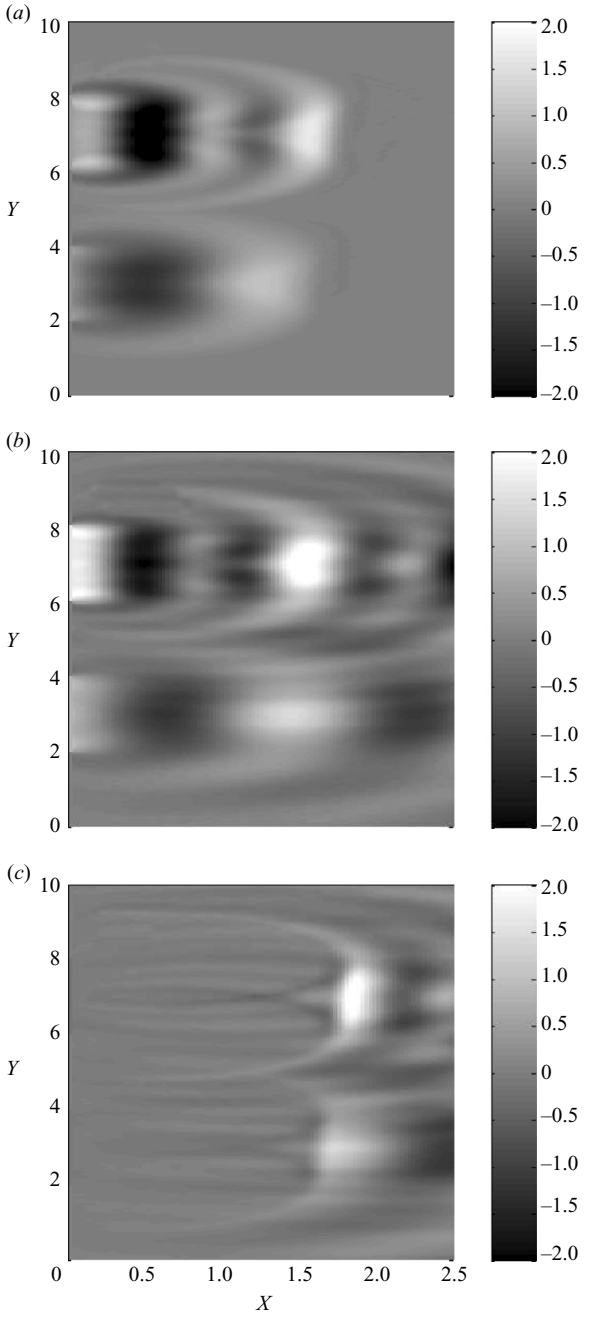

FIGURE 9. Direct simulation of the fluctuations of the pressure field $(p(x, y, t) - p_0)$ at three different times: (*a*) $t = 100\Delta t$, (*b*) $t = 300\Delta t$ and (*c*) $t = 600\Delta t$.

the spectrum of the acoustic disturbances. Figure 11 presents the imaginary part of the pressure field for the same three different times as in figure 10 but complex differentiation has been applied only to the frequency f_2 on the boundary. This is done in practice by filtering the signal stored on each boundary at the selected frequency. It is clearly observed that the sensitivity variable focuses on the only piston

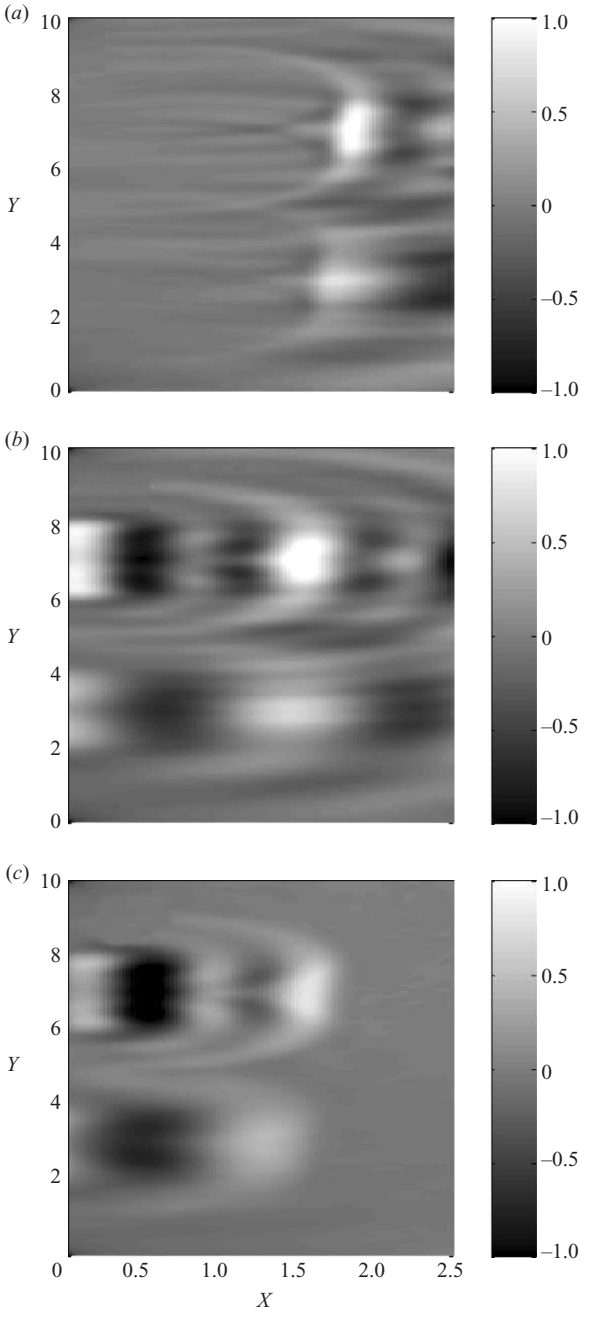

FIGURE 10. Imaginary part of the pressure field at three different times: (*a*) $\bar{t} = 400\Delta t$, (*b*) $\bar{t} = 700\Delta t$ and (*c*) $\bar{t} = 900\Delta t$.

which emits the frequency f_2. Therefore, it is shown that the present method allows to distinguish each contribution in the radiated acoustic spectrum and to localize the pistons locations accurately at each instant independently. That last ability is extensively used in the next section.

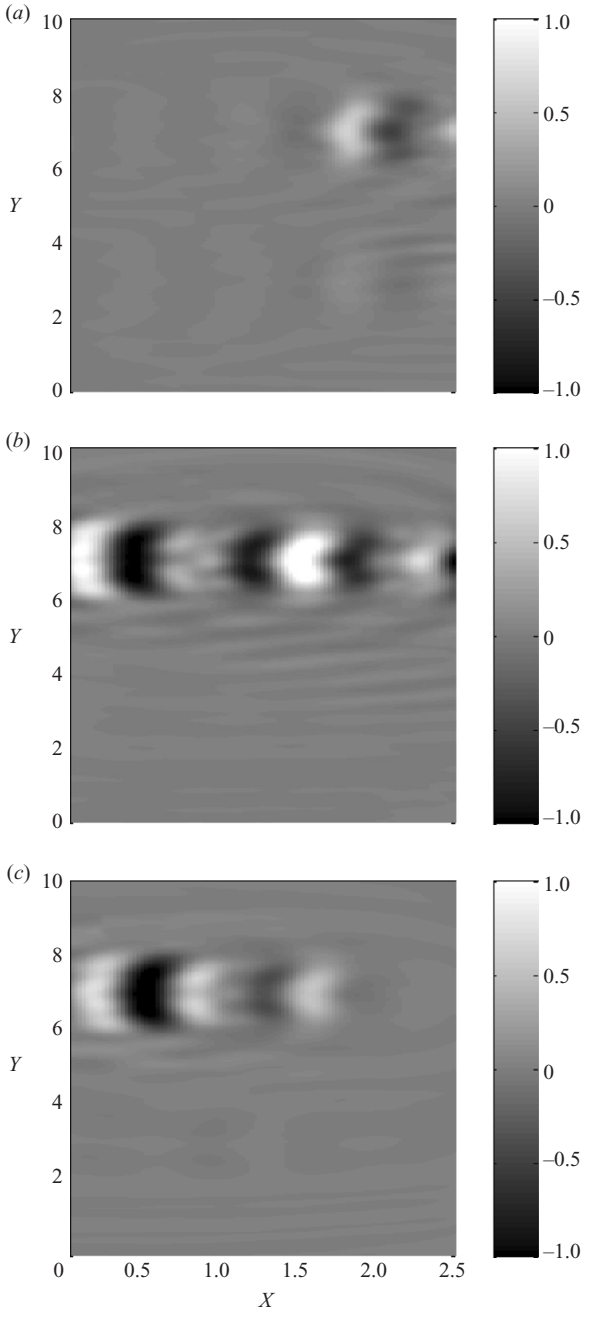

FIGURE 11. Imaginary part of the pressure field at three different times (*a*) $\bar{t} = 400\Delta t$, (*b*) $\bar{t} = 700\Delta t$ and (*c*) $\bar{t} = 900\Delta t$. The complex differentiation is used only on the frequency f_2.

3.3. *Sound generated by compressible plane mixing layer flow*

The purpose of this section is to apply the proposed methodology to localize regions associated with sound generation in a spatially developing shear flow in which the sound is generated by flow instabilities. The selected flow configuration is the

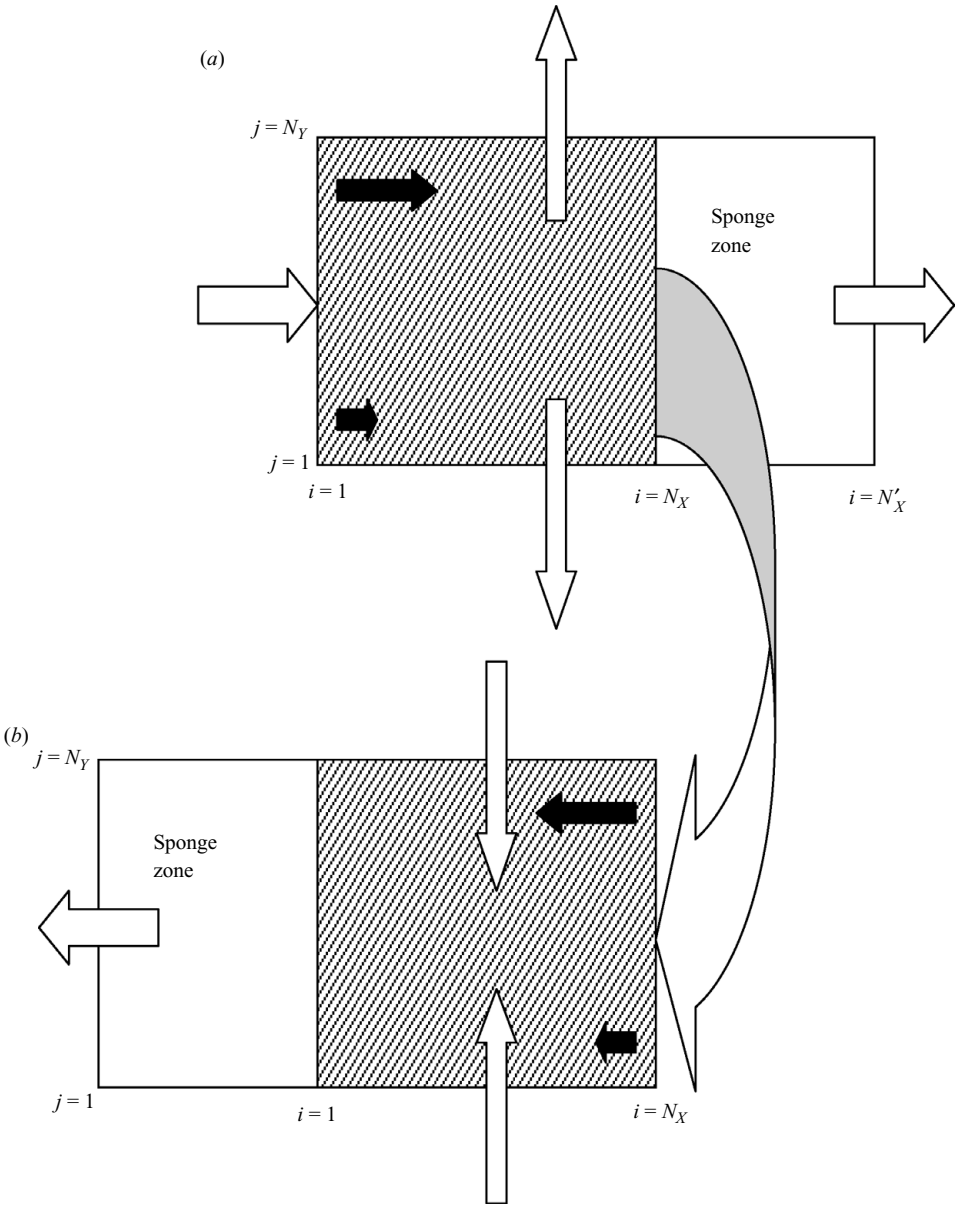

FIGURE 12. (*a*) First stage corresponding to the numerical simulation of the plane mixing layer. (*b*) Second stage corresponding to the time-reversed simulation using data stored at outflow boundaries in the first stage as inflow conditions. Black arrows indicate the mean streamwise flow direction. White arrows indicate the nature of the boundary conditions (inflow or outflow). Hachured zones correspond to the physical computational domain.

well-known subsonic two-dimensional plane mixing layer flow already analysed by Colonius *et al.* (1997). Such a flow that forms between merging fluid streams of different velocities is often regarded as the simplest form of free shear flows and the noise source mechanisms in such a flow have been intensively studied in the past (see Colonius *et al.* 1997; Bogey, Bailly & Juve 2000; Kleinman & Freund 2008; Druault *et al.* 2009).

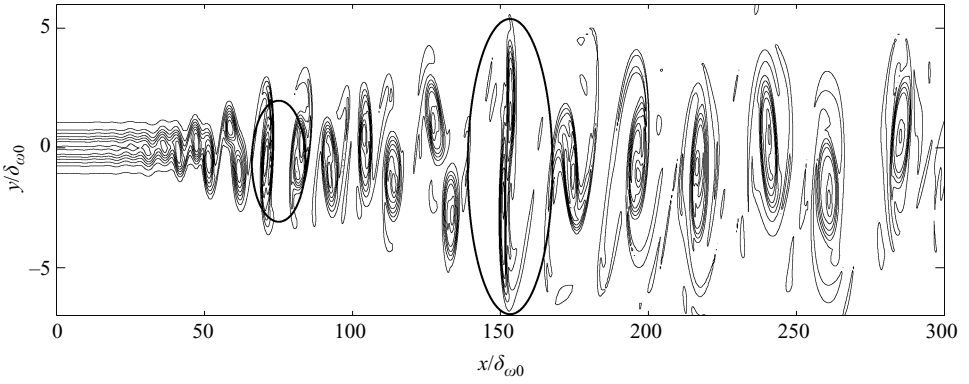

FIGURE 13. Instantaneous vorticity field in the near field mixing region.

The flow consists in two uniform streams with Mach numbers 0.5 and 0.25, respectively, for the upper and lower parts. The two regions are matched by a hyperbolic tangent profile for the streamwise velocity. Outflow conditions are specified at the top, the bottom and the left boundaries (see figure 12).

The physical domain (excluding the sponge region) is $(L_X, L_Y) = (350\delta_{\omega_0}, 350\delta_{\omega_0})$, where δ_{ω_0} is the inlet vorticity thickness. A uniform mesh with 1401×1401 grid points is used. A sponge layer zone is added to the computational domain in the streamwise direction to prevent spurious reflections (see figure 12). It ranges from $X = 350\delta_{\omega_0}$ to $X = 2500\delta_{\omega_0}$. In this zone, 200 grid points are used in the streamwise direction and the grid is stretched to damp fluctuations.

The numerical simulation is performed until a statistically stationary state is obtained. Once this state is obtained, the flow simulation is performed for 10 000 time steps, corresponding to more than one hundred periods of the fundamental frequency associated to the linearly most amplified mode predicted by the linear stability theory. The Strouhal number based on the fundamental frequency, the initial vorticity thickness and the convection velocity is 0.18.

The solution is recorded at each time step on all boundaries of the computational domain and at $X = 350\delta_{\omega_0}$ which is the exit boundary of the physical domain.

The flow is forced at the fundamental frequency predicted by the linear stability theory, f_0 and its first, second and third subharmonics. The inflow condition used on the left boundary ($X = 0$, $\forall Y$) is similar to the one used in Colonius *et al.* (1997). With such deterministic inflow perturbations, two quasi-stationary vortex pairings are observed within the computational domain. Moreover, to minimize the distance between both vortex pairings, the phase of the first subharmonics relative to the fundamental is imposed as it has previously been done (see Colonius *et al.* 1997).

An illustration of an instantaneous vorticity field is displayed in figure 13. Two pairing processes occur at $X \approx 75\delta_{\omega_0}$ and $X \approx 150\delta_{\omega_0}$, respectively. These locations are identical to those in Colonius *et al.* (1997) in a similar flow configuration. The corresponding pressure field is presented in figure 14, along with the acoustic pressure spectrum computed at the point $(275\delta_{\omega_0}, 175\delta_{\omega_0})$. Similar spectra are obtained at all boundaries. From the spectrum, various frequencies associated with the flow instabilities are clearly visible, but it is difficult to localize regions associated with sound generation at these frequencies just by looking at instantaneous fields.

The methodology presented above is now used. The time-reversal procedure is applied to all the variables stored on the top, the bottom and the right physical

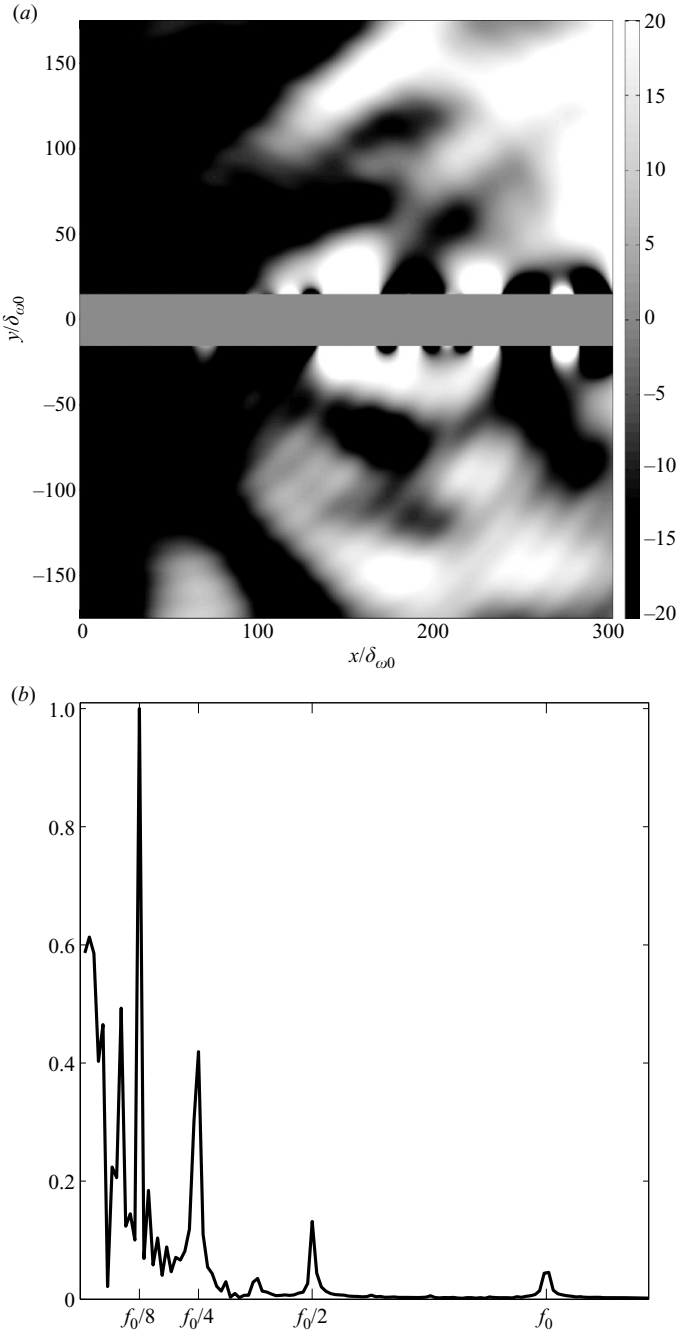

FIGURE 14. (*a*) Instantaneous far acoustic fluctuating pressure field. (*b*) Normalized pressure spectrum saved at the top boundary ($X = 275\delta_{\omega_0}$, $Y = 175\delta_{\omega_0}$).

boundaries. Data stored at the outlet of the sponge layer zone are not used since they are unphysical. Flow variables are then used as inflow conditions for the time-reversed simulation (see figure 12*b*). It is important to note that inflow conditions are now imposed on the top, the bottom and the right boundaries. A sponge zone is added on

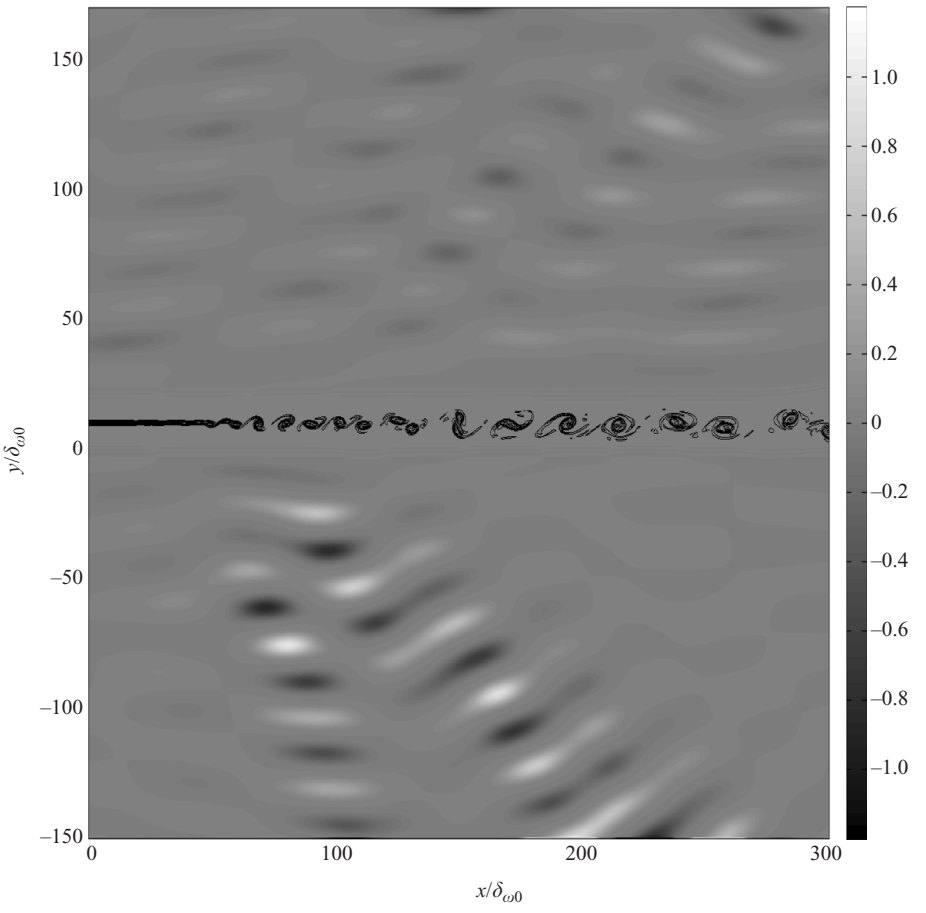

FIGURE 15. Instantaneous flow visualization of the imaginary part of the fluctuating pressure field associated with a filtering of $f_0/2$ superimposed onto the real vorticity field.

the left side of the physical domain, which is an outflow boundary for the time-reversed problem, to prevent any spurious reflection on this boundary. The computational grid is exactly the same as in the direct simulation. Contrary to the previous test cases, the localization of the regions associated with sound generation cannot be deduced directly from the information given by the time-reversed simulation, because of the strong coupling between aerodynamics and acoustics variables. Therefore, the complex differentiation technique is coupled to the time-reversal procedure to localize the area exhibiting the maximum sensitivity with respect to acoustical variables at a selected frequency. That frequency is identified from the spectrum measured at the boundaries of the computational domain. Thus, a small imaginary part is added to the acoustic pressure used in the inflow condition of the time-reversed simulations at the frequency under consideration. This is simply done by filtering the acoustic pressure stored on the computational boundaries during the direct simulation and filtering it at the target frequency using Fourier transform. The resulting filtered signal is then multiplied by $i\epsilon$ and added to the original signal used to define inflow conditions for the time-reversed simulation.

Two time-reversed simulations are performed to extract the zones with the maximum sensitivity with respect to acoustical variables at the subharmonic

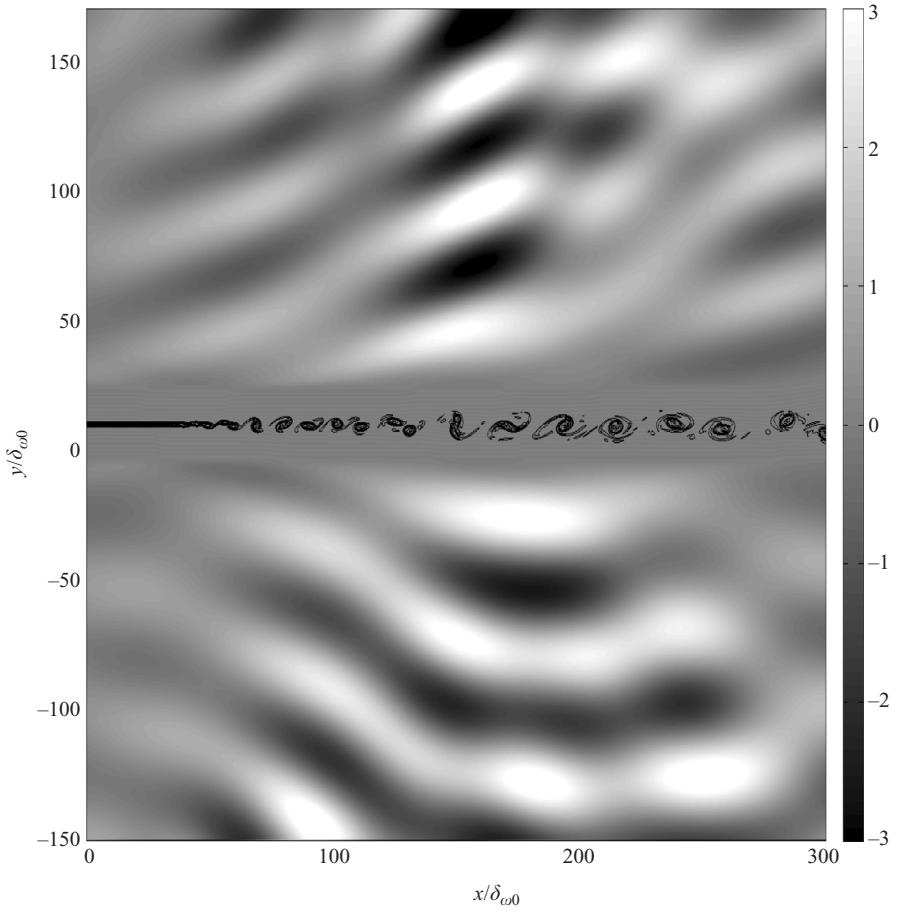

FIGURE 16. Instantaneous flow visualization of the imaginary part of the fluctuating pressure field associated with a filtering of $f_0/4$ superimposed onto the real vorticity field.

frequencies $f_0/2$ and $f_0/4$. These zones correspond directly to the maximum of the imaginary part of the different fields. Figures 15 and 16 display the imaginary part of the pressure field (i.e. the sensitivity of the acoustic pressure) associated with these two frequencies, at the same time. In these figures, the corresponding instantaneous vorticity field coming from the direct simulation is also provided. It can be observed that imaginary part of the pressure waves associated with $f_0/2$ and $f_0/4$ frequencies converge towards the first and second pairing locations, respectively (see figure 13). According to the complex differentiation technique, the imaginary part can be associated to the sensitivity with respect to acoustical variables. Thus, the area the more sensitive in the time-reversed simulation correspond to regions associated with sound generation in the direct computation.

Such a visual localization procedure is useful but may be inefficient in more complex flows. To obtain a more systematic localization the root mean square (r.m.s.) of the pressure sensitivity is computed (see figures 17 and 18), leading to a hybrid statistical-sensitivity identification procedure of the regions associated with sound generation, in the spirit of previous works based on the adjoint solution (see Colonius & Lele 2004 for a general discussion). Maxima of the r.m.s. sensitivity of acoustic pressure

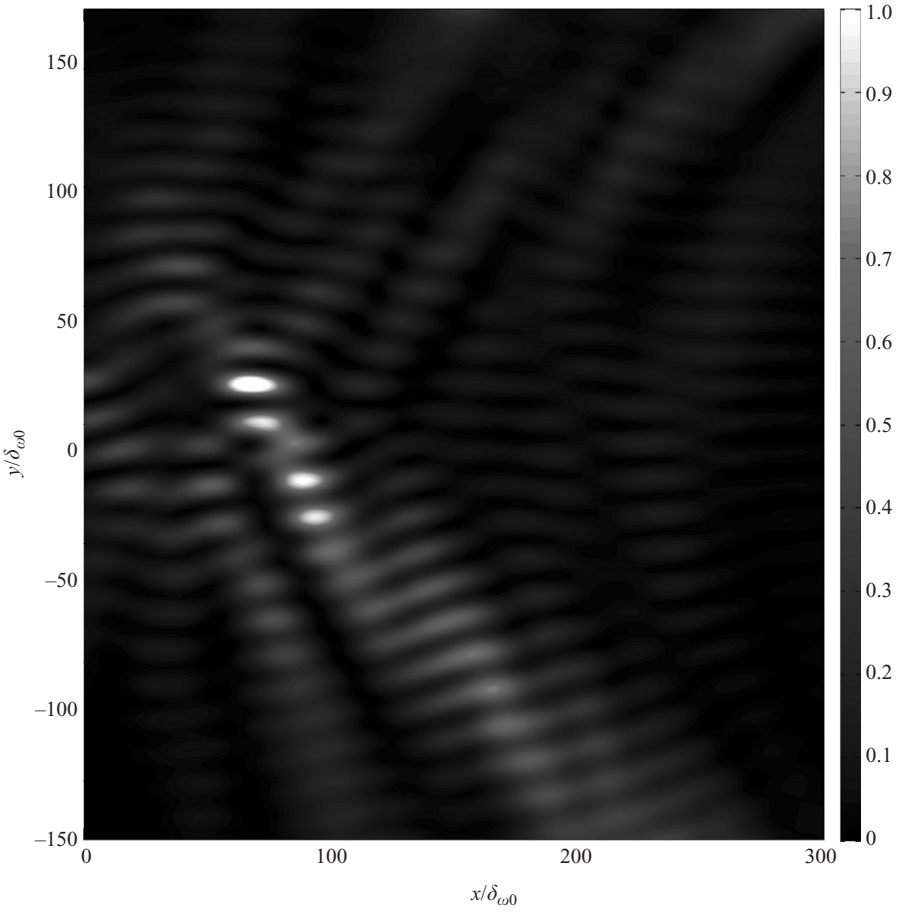

FIGURE 17. Root mean square of the first derivative of the complex pressure field associated with a filtering of $f_0/2$.

are clearly seen in the mixing layer near $X = 75\delta_{\omega_0}$ and $X = 150\delta_{\omega_0}$. These locations correspond to the locations of the first and second pairings (figure 13). Beyond the localization of the regions associated with sound generation, figures 17 and 18 provide additional information. In both cases, the repartition of the pressure field looks like a longitudinal quadrupole. The axis of the quadrupole is perpendicular to the flow direction. Indeed, on each figure, four distinct spots of r.m.s. pressure are higher than the others. The size of the quadrupoles in the Y direction corresponds approximatively to two wavelengths (about 50 for $f_0/2$ and 100 for $f_0/4$) and is approximately one wavelength in the X direction. This size is important compared to the vorticity thickness which is the characteristic size of the plane mixing layer. Nevertheless, the characteristic scale of the acoustic problem is the wavelength. It is well known that the resolution for the retrofocusing, in medical-imaging for instance, is given by the wavelength (a subwavelength resolution can be reach only under certain circumstances). Consequently, the observed sizes of the regions of maximum sensitivity are consistent compared to classical sizes of regions associated with the generation of sound at frequencies $f_0/2$ and $f_0/4$. Moreover, these results are in agreement with the quadripolar nature of aeroacoustic sources predicted by the

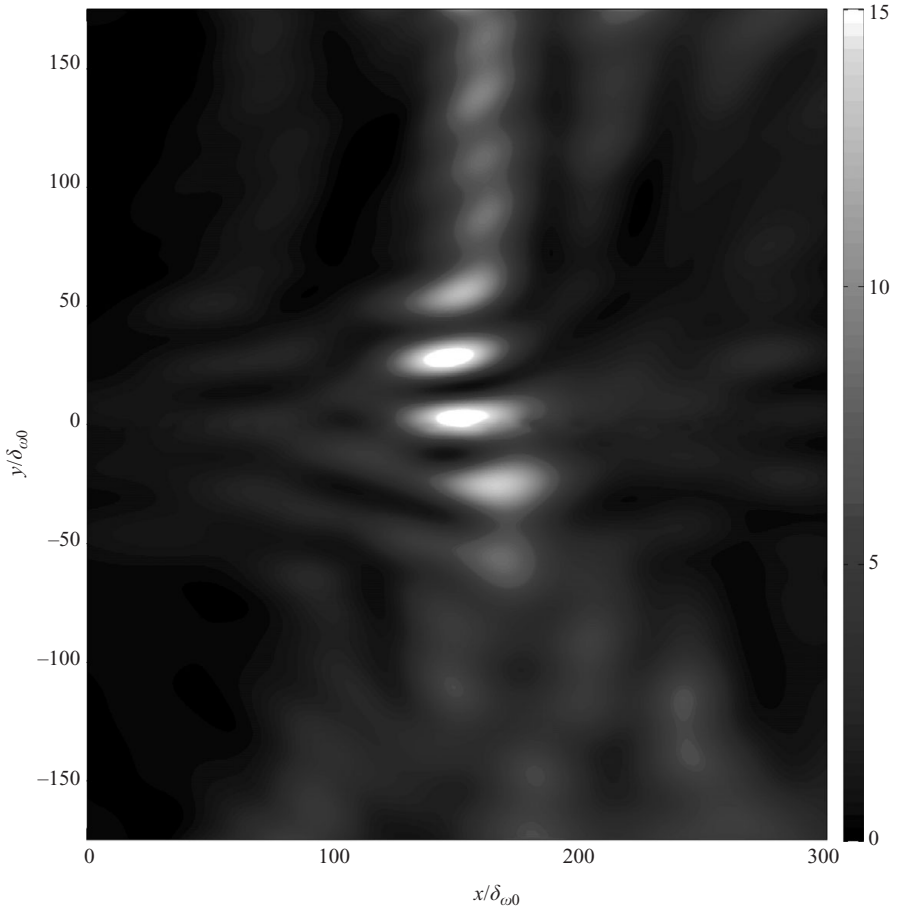

FIGURE 18. Root mean square of the first derivative of the complex pressure field associated with a filtering of $f_0/4$.

Lighthill's analogy (Lighthill 1952). Of course, that observation is not a formal proof of the equivalence between the Lighthill's analogy and the resolution of the inverse problem but from our point of view it is important to outline that similar conclusion between both approaches. Note that in the proposed methodology, those results are obtained from the resolution of the inverse problem and do not originate in an *a priori* model. Moreover, they are no assumptions on the nature of the flow. All the methodology is systematic without any adjustable parameters.

4. Concluding remarks

An original methodology for the detection of regions associated with high sensitivity of the radiated noise has been proposed and assessed. It relies on the efficient coupling between the time-reversal theory applied to the Euler equations and the complex differentiation method to compute the sensitivity variables. This methodology has been validated by various test cases. First of all, it has been demonstrated that it is possible to localize accurately the wavefront up to the initial position of the sound generated by an injection of mass, even in the presence of strong scattering effects. Then, the methodology has been applied to the detection of vibrating surfaces. In

this case, it is possible to localize easily the position of the piston responsible of the radiation of sound at a particular frequency thanks to the complex differentiation. Finally, the methodology has been used to find the regions associated with sound generation in a plane mixing layer.

The proposed methodology is observed to be a robust and accurate process to detect regions associated with sound generation. No assumptions on the nature of the flow are needed. The methodology is systematic and without any adjustable parameters. Thus, results are computed only from the resolution of the inverse problem without any assumption. The methodology can be extended to more complex geometries such as curvilinear grids or three-dimensional flow configurations.

REFERENCES

Anderson, W. K., Newman, J. C., Whitfield, D. L. & Nielsen, E. J. 2001 Sensitivity analysis for the Navier–Stokes equations on unstructured meshes using complex variables. *AIAA J.* **1**, 56–63.

Barone, M. F. & Lele, S. K. 2005 Receptivity of the compressible mixing layer. *J. Fluid Mech.* **540**, 301–335.

Bogey, C. & Bailly, C. 2007 An analysis of the correlations between the turbulent flow and the sound pressure fields of subsonic jets. *J. Fluid Mech.* **583**, 71–91.

Bogey, C., Bailly, C. & Juve, D. 2000 Numerical simulation of sound generated by vortex pairing in a mixing layer. *AIAA J.* **40** (2), 235–243.

Cassereau, D. & Fink, M. 1992 Time-reversal of ultrasonic fields. III. Theory of the closed time-reversal cavity. *IEEE Trans. Ultrason. Ferroelectr. Freq. Control* **39** (5), 579–592.

Colonius, T. & Lele, S. K. 2004 Computational aeroacoustics: progress on nonlinear problems of sound generation. *Prog. Aerosp. Sci.* **40** (6), 345–416.

Colonius, T., Lele, S. K. & Moin, P. 1994 The scattering of sound waves by a vortex numerical simulations and analytical solutions. *J. Fluid Mech.* **260**, 271–298.

Colonius, T., Lele, S. K. & Moin, P. 1997 Sound generation in a mixing layer. *J. Fluid Mech.* **330**, 375–409.

Dowling, A. P. & Ffwocs Williams, J. E. 2000 *Sound and Sources of Sound*. Ellis Horwood.

Druault, Ph., Yu, M. & Sagaut, P. 2009 Quadratic stochastic estimation of far field acoustic pressure with coherent structure events in a 2D compressible plane mixing layer. *Intl J. Numer. Methods Fluids*, doi:10.1002/fld.2047 (in press).

Fink, M., Cassereau, D., Derode, A., Prada, C., Roux, P., Tanter, M., Thomas, J.-L. & Wu, F. 2000 Time-reversed acoustics. *Prog. Rep. Phys.* **63**, 1933–1995.

Goldstein, M. E. 1976 *Aeroacoustics*. McGraw-Hill.

Goldstein, M. E. 2003 A generalized acoustic analogy. *J. Fluid Mech.* **488**, 315–333.

Goldstein, M. E. & Leib, S. J. 2008 The aeroacoustics of slowly diverging supersonic jets. *J. Fluid Mech.* **600**, 291–337.

Howe, M. S. 2003 *Theory of Vortex Sound*. Cambridge Texts in Applied Mathematics, vol. 33. Cambridge University Press.

Jameson, A., Martinelli, L. & Pierce, N. 1998 Optimum aerodynamic design using the Navier–Stokes equations. *J. Theor. Comput. Fluid Dyn.* **10**, 213–237.

Jordan, P. & Gervais, Y. 2008 Subsonic jet aeroacoustics: associating experiment, modelling and simulation. *Exp. Fluids* **44** (1), 1–21.

Kleinman, R. R. & Freund, J. B. 2008 The sound from mixing layers simulated with different ranges of turbulence scales. *Phys. Fluids* **20**, 101503.

Kovasznay, L. S. G. 1953 Turbulence in supersonic flow. *J. Aeronaut. Soc.* **20** (10), 657–682.

Leclerc, E., Sagaut, P. & Mohammadi, B. 2006 On the use of incomplete sensitivities for feedback control of laminar vortex shedding. *Comput. Fluids* **35** (10), 1432–1443.

Lighthill, M. J. 1952 On sound generated aerodynamically: I. General theory. *Proc. R. Soc. Lond.* **211**, 564–587.

Lighthill, M. J. 1978 *Waves in Fluids*. Cambridge University Press.

Lilley, G. M. 1974 On the noise from jets. *AGARD* **CP-131**, 13.1–13.12.

Lu, S. Y. & Sagaut, P. 2007*a* Direct sensitivity analysis for smooth unsteady compressible flows using complex differentiation. *Intl J. Numer. Methods Fluids* **53**, 1863–1886.

Lu, S. Y. & Sagaut, P. 2007*b* Pseudo-characteristic formulation and dynamic boundary conditions for computational aeroacoustics. *Intl J. Numer. Methods Fluids* **53**, 201–227.

Lund, F. & Rojas, C. 1989 Ultrasound as probe of turbulence. *Physica* D **37**, 508–514.

Lyness, J. N. & Moler, C. B. 1967 Numerical differentiation of analytic functions. *SIAM J. Numer. Anal.* **4**, 202–210.

Peake, N. 2004 A note on "Computational aeroacoustics examples showing the failure of the acoustic analogy theory to identify the correct noise sources" by CKW Tam. *J. Comput. Acoust.* **12** (4), 631–634.

Pierce, A. D. 1989 *Acoustics, an Introduction to Its Physical Principles and Applications*. Acoustical Society of America.

Roux, P. & Fink, M. 1995 Experimental evidence in acoustics of the violiation of time-reversal invariance induced by vorticity. *Europhys. Lett.* **32**, 25–29.

Roux, P., de Rosny, J., Tanter, M. & Fink, M. 1997 The Aharonov–Bohm effect revisited by an acoustic time reversal mirror. *Phys. Rev. Lett.* **79**, 3170–3173.

Sagaut, P. & Cambon, C. 2008 *Homogeneous Turbulence Dynamics*. Cambridge University Press.

Sesterhenn, J. 2001 A characteristic-type formulation of the Navier–Stokes equations for high order upwind schemes. *Comput. Fluids* **30**, 37–67.

Shu, C. W. & Osher, S. 1989 Efficient implementation of essentially non-oscillatory shock capturing schemes. *J. Comput. Phys.* **83**, 32–78.

Spagnoli, B. & Airiau, C. 2008 Adjoint analysis for noise control in a two-dimensional compressible mixing layer. *Comput. Fluids* **37**, 475–486.

Spalart, R. P. 2007 Application of full and simplified acoustic analogies to an elementary problem. *J. Fluid Mech.* **578**, 113–118.

Squire, W. & Trapp, G. 1998 Using complex variables to estimate derivatives of real functions. *SIAM Rev.* **10** (1), 110–112.

Tam, C. K. W. 2002 Computational aeroacoustics examples showing the failure of the acoustic analogy theory to identify the correct noise sources. *J. Comput. Acoust.* **10** (4), 387–405.

Tam, C. K. W. & Auriault, L. 1998 Mean flow refraction effects on sound radiated from localized sources in a jet. *J. Fluid Mech.* **370**, 149–170.

Vatsa, V. N. 2000 Computation of sensitivity derivatives of Navier–Stokes equations using complex variables. *Adv. Engng Softw.* **31** (8-9), 655–659.

Wagner, C., Hüttl, T. & Sagaut, P. (ed.) 2007 *Large-Eddy Simulation for Acoustics*. Cambridge University Press.

Wang, M., Freund, J. B. & Lele, S. K. 2006 Computational prediction of flow-generated sound. *Annu. Rev. Fluid Mech.* **38**, 483–512.

Wei, M. J. & Freund, J. B. 2006 A noise-controlled free shear flow. *J. Fluid Mech.* **546**, 123–152.